Moment–based boundary conditions for lattice Boltzmann simulations of natural convection in cavities

Rebecca Allen

Division of Physical Science and Engineering,
King Abdullah University of Science and Technology,
Thuwal,
Saudi Arabia.   E-mail: rebecca.allen@kaust.edu.sa

Tim Reis

School of Computing and Mathematics,
Plymouth University,
UK.   E-mail: timothy.reis@plymouth.ac.uk

Abstract: We study a multiple relaxation time lattice Boltzmann model for natural convection with moment–based boundary conditions. The unknown primary variables of the algorithm at a boundary are found by imposing conditions directly upon hydrodynamic moments, which are then translated into conditions for the discrete velocity distribution functions. The method is formulated so that it is consistent with the second order implementation of the discrete velocity Boltzmann equations for fluid flow and temperature. Natural convection in square cavities is studied for Rayleigh numbers ranging from 10^3 to 10^8. An excellent agreement with benchmark data is observed and the flow fields are shown to converge with second order accuracy.

Keywords: Lattice Boltzmann, moment–based boundary conditions, natural convection, multiple relaxation times

1 Introduction

Natural convection occurs in a diverse range of phenomena, from thermal flows in the atmosphere [42] to small scale microfluidics [28]. Its significance has generated much interest in the scientific and engineering communities, including computational fluid dynamics (CFD) (see, for example, [10, 35, 26, 32, 25, 9]). The classic benchmark test for numerical methods is thermal flow in a square cavity comprised of two adiabatic horizontal walls (*i.e.*, Neumann boundary conditions) and two thermally fixed vertical walls (*i.e.*, Dirichlet boundary conditions), where the left wall is hotter than the right. This flow is dictated by two non–dimensional numbers, namely the Prandtl number, Pr, and Rayleigh number, Ra. The Prandtl number is the ratio of momentum to thermal diffusivity; the value $Pr = 0.71$ is generally taken for air, and $Pr = 7$ represents water near room temperature.

The onset of convection is determined by the critical Rayleigh number and its magnitude indicates whether the convection boundary layer is laminar or turbulent.

Traditional algorithms involve a direct discretisation of the highly non–linear partial differential equations of continuum fluid mechanics, namely the Navier–Stokes equations with a Boussinesq approximation for the buoyancy. An alternative to the more familiar methods of CFD is the lattice Boltzmann equation (LBE), which is based on a velocity–space truncation of the Boltzmann equation of classical kinetic theory [21]. By seeking solutions which vary slowly over hydrodynamic timescales much longer than the collision time, τ_ν, the (lattice) Boltzmann equation can be shown to approximate the Navier–Stokes equations [5, 39, 20]. This seemingly indirect method offers several computational advantages. The non–linear convection term in the macroscopic equations is replaced by linear, constant coefficient advection in the discrete velocity Boltzmann equation. Furthermore, all non–linearities are confined to an algebraic source term which can be updated locally, grid–point by grid–point. The locality of the algorithm allows for a natural parallelisation on modern computer architectures [6, 45, 1].

The application of the lattice Boltzmann model to thermal flows began two decades ago [2, 3, 15]. Alexander *et al.* [2] adopted a multi-speed approach to study Couette flow with an imposed temperature gradient and Bartoloni *et al.* [3] studied Rayleigh-Bénard convection by modelling the temperature as a passive scalar. To improve the numerical stability of thermal lattice Boltzmann models, McNamara *et al.* [36] used a Lax–Wendroff scheme to discretise the advection term. This method introduces greater artificial viscosity and the authors conclude that their method offered no advantages over finite difference methods.

Shan [41] studied Rayleigh-Bénard convection using a lattice Boltzmann model with two distribution functions, one for the fluid flow and another for the thermal transport. By comparing their simulation results with those of Clever and Busse [9], the authors concluded that the steady-state Nusselt numbers were in good agreement for $Ra < 20000$, but deviated at higher values. He *et al.* [19] evolved the temperature by an internal energy distribution function, rather than a passive-scalar approach. Similar to the model of Shan [41], this method was able to make predictions in good agreement with Clever and Busse's [9] benchmark simulations for $Ra < 20000$ but gave quantitatively incorrect results at higher Rayleigh numbers.

Dixit *et al.* [14] combined the 'double-population' approach of He *et al.* [19] with both an interpolation-supplemented method [22] and an extension to Inamuro's counter–slip technique [27] to accurately incorporate the boundary conditions. Laminar flow simulations were compared to the benchmark solution of de Vahl Davis [10] and an agreement within 3% noticed. Turbulent flow simulations at Rayleigh numbers between 10^7 and 10^{10} were within a 5% agreement when compared to Le Quere [32] and Markatos et al. [35]. The authors credited their model's accuracy to the their very fine grid resolution at the wall boundary.

The models of Guo *et al.* [17, 18] consist of two independent LBEs (one for hydrodynamics, one for the temperature) on separate lattices which are coupled together through a term added to the fluid distribution function. Li *et al.* [33] presented a coupled lattice Boltzmann model for thermal flows based on the double-distribution function of Guo *et al.* [18] using both the Bhatnagar–Gross–Krook (BGK) and multiple–relaxation–time (MRT) collision schemes. Their results show that the MRT collision operator offers greater numerically stability than the BGK scheme.

Hybrid thermal lattice Boltzmann models have been proposed or studied by Lallemand *et al.* [31], Mezrhab *et al.* [37], and Choi and Kim [7]. Lallemand *et al.* [31] argued that

previous thermal lattice Boltzmann models were based on a spurious coupling between the viscous and energy modes. To circumvent this, they evolved the hydrodynamics using an LBE and the temperature field using a finite difference algorithm.

Wang *et al.* [44] presented a thermal lattice Boltzmann model with multiple relaxation times for both the fluid and transport equations. The anti-bounce-back method is used to implement Dirichlet boundary conditions and bounce-back for the Neumann boundary conditions. The authors compared their results with several other methods in the literature [10, 26, 32, 17, 37] and provided the most detailed study of a lattice Boltzmann model for natural convection to date. By computing the L_2 error norm for the flow fields (velocity, pressure, and temperature) Wang *et al.* [44] showed their algorithm converges with second order in space. The computed Nusselt numbers are in good agreement with benchmark solutions for a range of Rayleigh numbers and the authors emphasised the importance of using multiple relaxation times.

Part of the motivation for using multiple relaxation times in [44] is to eliminate the numerical slip error that plagues the bounce–back boundary condition method [16, 24]. That is, the collision time for the third order moment is chosen so that, as accurately as possible, $\mathbf{u} = 0$ at the walls. This places an additional restriction on the collision operator. Ideally one would choose the relaxation times purely on grounds of numerical stability and not according to the boundary conditions. In particular, the value of the collision time for the third order moment needed to minimise the numerical slip error is not necessarily optimal [13].

Similar in spirit to the original work of Noble *et al.* [38], Bennett [4] proposed a general methodology for implementing lattice Boltzmann boundary conditions in terms of the moments of the distribution functions. Unlike bounce-back and its variants, this 'moment–method' assumes a wall to be located precisely at grid points. The method remains fully local and does not require any additional finite difference approximations nor any interpolation/extrapolation of quantities to or from neighbouring nodes. The drawback of the approach is evident: a lack of flexibility for flows in complicated geometries. It does, however, guarantee the satisfaction of hydrodynamic quantities at the boundaries, allowing for greater freedom in the choice of relaxation times. It is thus natural to inquire if the moment–method can be applied to natural convection and, if so, to assess its accuracy.

In this article we develop lattice Boltzmann boundary conditions for natural convection in the framework of the moment–method. We use a second–order–in–time discretisation [23] of two discrete velocity Boltzmann equations, one for the fluid flow and one for the thermal transport, coupled through a force term for the buoyancy (Boussinesq approximation). A multiple relaxation time collision operator is used for each, where the collision time for the third order moment of the fluid LBE is chosen according to numerical stability and the collision times for the thermal transport chosen so that the numerical diffusion is isotropic to fourth order [31]. The boundary conditions are imposed on the moments of each distribution function, and then translated into conditions for the primary variables of the algorithm. Our implementation does not lose the computational advantages of the lattice Boltzmann method and inherits its second order accuracy. The proposed model is assessed with the classic benchmark test of convection in a square cavity for Rayleigh numbers ranging from 10^3 to 10^8. It is also shown how the moment–method can be applied to the industrially-relevant problem of convection in partially open geometries.

The remainder of the article is organised as follows: Section 2 introduces the governing macroscopic equation of motion and Section 3 presents the lattice Boltzmann formulation of the problem. Section 4 develops the moment–based boundary conditions, and the multiple

relaxation time extension is discussed in Section 5. Numerical simulations of convection in a square cavity are presented in Sections 6 and 7, and for a partially heated cavity in Section 8. Concluding remarks are left to Section 9.

2   Governing macroscopic equations

Natural convection is a buoyancy-driven flow which can be modelled with the Boussinesq approximation. This approximation assumes that density variations due to temperature can be neglected in all but the gravitational acceleration term, which is included as a body force in the Navier–Stokes equations,

$$\rho\Big[\frac{\partial \mathbf{u}}{\partial t} + \mathbf{u}\cdot\nabla\mathbf{u}\Big] = -\nabla P + \mu\nabla^2\mathbf{u} + \mathbf{F}, \tag{1}$$

$$\nabla\cdot\mathbf{u} = 0, \tag{2}$$

where ρ is the density, $\mathbf{u}$ is the flow velocity, P is pressure, μ is the dynamic viscosity, and $\mathbf{F}$ is the body force acting on the fluid. This force is given by $\mathbf{F} = \rho\alpha(\phi - \phi_0)\mathbf{g}$, where α is the thermal expansion coefficient, ϕ and ϕ_0 are the temperature and reference temperature, respectively, and $\mathbf{g} = (0, g)$ is the gravitational acceleration. The temperature evolves according to the advection–diffusion equation,

$$\frac{\partial \phi}{\partial t} + \mathbf{u}\cdot\nabla\phi = D\nabla^2\phi, \tag{3}$$

where D is the thermal diffusion coefficient.

   Equations (1)–(3) are non–dimensionalised by scaling

$$t' = t\frac{D}{L^2}, \quad \mathbf{x}' = \frac{\mathbf{x}}{L}, \quad \mathbf{u}' = \frac{\mathbf{u}L}{D}, \quad P' = P\frac{L^2}{\rho D^2}, \quad \theta = \frac{(\phi - \phi_0)}{\Delta\phi}, \tag{4}$$

where $\Delta\phi$ is the temperature difference (between the hot and cold walls in this study). Defining the Prandtl and Rayleigh numbers to be

$$Pr = \frac{\nu}{D}, \quad Ra = \frac{\alpha g\Delta\phi L^3}{\nu D}, \tag{5}$$

allows us to write the governing equations in non-dimensional form:

$$\frac{\partial \mathbf{u}}{\partial t} + \mathbf{u}\cdot\nabla\mathbf{u} = -\nabla P + Pr\nabla^2\mathbf{u} + RaPr\theta\hat{\mathbf{g}}; \tag{6}$$

$$\nabla\cdot\mathbf{u} = 0; \tag{7}$$

$$\frac{\partial \theta}{\partial t} + \mathbf{u}\cdot\nabla\theta = \nabla^2\theta, \tag{8}$$

where $\hat{\mathbf{g}}$ is a unit vector in the vertical direction and we have omitted primes for clarity. The kinematic viscosity, ν, and the diffusion coefficient, D, are given in terms of the non–dimensional numbers:

$$\nu = \sqrt{\frac{\alpha g\Delta\phi L^3 Pr}{Ra}}; \quad D = \sqrt{\frac{\alpha g\Delta\phi L^3}{PrRa}}. \tag{9}$$

The characteristic velocity of the flow is

$$U = \sqrt{\alpha g \Delta \phi L}. \tag{10}$$

The flow physics in natural convection are controlled by Pr and Ra. Small Prandtl number flows, such as for air ($Pr = 0.71$), are dominated by thermal diffusion, while large Prandtl numbers ($Pr = 7$ for water near room temperature) correspond to momentum diffusion dominated flows. The onset of convection is governed by the Rayleigh number, where beyond some critical value the flow exhibits a Rayleigh–Bénard instability and the primary form of thermal transport changes from conduction to convection.

3 The discrete Boltzmann formulation

We postulate two discrete velocity Boltzmann equations (DBEs), one to describe the evolution of the fluid flow (f_i) and another for thermal transport (g_i):

$$\frac{\partial f_i}{\partial t} + \mathbf{c}_i \cdot \nabla f_i = -\frac{1}{\tau_\nu} \left(f_i - f_i^{(eq)} \right) + R_i, \tag{11}$$

$$\frac{\partial g_i}{\partial t} + \mathbf{c}_i \cdot \nabla g_i = -\frac{1}{\tau_D} \left(g_i - g_i^{(eq)} \right), \tag{12}$$

where τ_ν and τ_D are the relaxation times associated with viscous and thermal diffusion, respectively, and R_i is the forcing term. The discrete particle velocity set $\{\mathbf{c}_i\}$ for f_i is the D2Q9 lattice shown in Figure 1, while that for the (linear) advection–diffusion equation is the D2Q5 lattice model ($i = 0, \ldots 4$). The equilibrium functions $f_i^{(eq)}$ and $g_i^{(eq)}$ are given by

$$f_i^{(eq)} = W_i \rho \left[1 + 3\mathbf{c}_i \cdot \mathbf{u} + \frac{9}{2} \left(\mathbf{c}_i \cdot \mathbf{u} \right)^2 - \frac{3}{2} \mathbf{u}^2 \right], \tag{13}$$

$$g_i^{(eq)} = T_i \phi \left[1 + 3\mathbf{c}_i \cdot \mathbf{u} \right], \tag{14}$$

where the weights are $W_0 = 4/9$, $W_i = 1/9$ for $i = 1, \ldots, 4$, $W_i = 1/36$ for $i = 5, \ldots, 8$, and $T_0 = 1/3$, $T_i = 1/6$ for $i = 1, \ldots, 4$.

The source term R_i introduces the body force $\mathbf{F}$ and must satisfy

$$\sum_i R_i = 0, \quad \sum_i R_i \mathbf{c}_i = \mathbf{F}, \quad \sum_i R_i \mathbf{c}_i \mathbf{c}_i = \mathbf{F}\mathbf{u} + \mathbf{u}\mathbf{F}. \tag{15}$$

The first constraint in (15) is a statement of mass conservation and the second accounts for the buoyancy effect. The third condition ensures $\mathbf{F}$ does not appear in the viscous stress term in the Navier–Stokes equations (26). The explicit form of R_i is [34]

$$R_i = 3W_i \left[(\mathbf{c}_i - \mathbf{u}) + 3\mathbf{c}_i \cdot \mathbf{u}\mathbf{c}_i \right] \cdot \mathbf{F}. \tag{16}$$

The hydrodynamic quantities, namely fluid density (ρ), momentum ($\rho\mathbf{u}$), momentum flux ($\mathbf{\Pi}$), thermal density (ϕ), and thermal flux ($\mathbf{\Psi}$) are defined by moments of the distribution functions:

$$\rho = \sum_{i=0}^{8} f_i; \quad \rho\mathbf{u} = \sum_{i=0}^{8} f_i \mathbf{c}_i; \quad \mathbf{\Pi} = \sum_{i=0}^{8} f_i \mathbf{c}_i \mathbf{c}_i; \tag{17}$$

$$\phi = \sum_{i=0}^{4} g_i; \quad \mathbf{\Psi} = \sum_{i=0}^{4} g_i \mathbf{c}_i. \tag{18}$$

Taking the 0th-, 1st-, and 2nd-order moments of equation (11) yields

$$\frac{\partial \rho}{\partial t} + \nabla \cdot \rho \mathbf{u} = 0, \tag{19}$$

$$\frac{\partial \rho \mathbf{u}}{\partial t} + \nabla \cdot \mathbf{\Pi} = \mathbf{F}, \tag{20}$$

$$\frac{\partial \mathbf{\Pi}}{\partial t} + \nabla \cdot \mathbf{Q} = -\frac{1}{\tau_\nu} (\mathbf{\Pi} - \mathbf{\Pi}^{(eq)}). \tag{21}$$

Equations (19) and (20) are the conservation laws for mass and momentum (with a body force). The momentum flux, $\mathbf{\Pi}$, is not conserved by collisions and relaxes to equilibrium $\mathbf{\Pi}^{(eq)} = \sum_i f_i^{(eq)} \mathbf{c}_i \mathbf{c}_i$ according to its own partial differential equation (21). The third order moment in equation (21) is given by $\mathbf{Q} = \sum_i f_i \mathbf{c}_i \mathbf{c}_i \mathbf{c}_i$.

The Navier–Stokes equations can be obtained from the discrete Boltzmann equation (11) by looking for solutions that vary slowly over timescales much longer than the collision time τ_ν [5]. Using the Chapman-Enskog expansion,

$$\frac{\partial}{\partial t} = \frac{\partial}{\partial t_0} + \tau_\nu \frac{\partial}{\partial t_1} + ..., \tag{22}$$

$$\mathbf{\Pi} = \mathbf{\Pi}^{(0)} + \tau_\nu \mathbf{\Pi}^{(1)} + ..., \tag{23}$$

$$\mathbf{Q} = \mathbf{Q}^{(0)} + \tau_\nu \mathbf{Q}^{(1)} + ..., \tag{24}$$

we find the (weakly compressible) Navier–Stokes equations to leading order,

$$\frac{\partial \rho}{\partial t} + \nabla \cdot \rho \mathbf{u} = 0, \tag{25}$$

$$\frac{\partial \rho \mathbf{u}}{\partial t} + \nabla \cdot \left(\mathbf{\Pi}^{(0)} + \tau_\nu \mathbf{\Pi}^{(1)} \right) = 0, \tag{26}$$

where

$$\mathbf{\Pi}^{(0)} = P\boldsymbol{I} + \rho \mathbf{u}\mathbf{u}, \tag{27}$$

$$\mathbf{\Pi}^{(1)} = -\frac{1}{3} \rho \left(\nabla \mathbf{u} + (\nabla \mathbf{u})^T \right) + \mathcal{O}(Ma^3), \tag{28}$$

and $Ma =$ is the Mach number. The kinematic viscosity is seen to be a function of the relaxation time, $\nu = \tau_\nu/3$, and the pressure is given by an ideal equation of state, $P = \rho/3$.

A similar procedure applied to the discrete Boltzmann equation (12) for g_i with the expansion $\mathbf{\Psi} = \mathbf{\Psi}^{(eq)} + \tau_D \mathbf{\Psi}^{(1)} + \ldots$, yields at leading order the convection–diffusion equation

$$\frac{\partial \phi}{\partial t} + \nabla \cdot (\phi \mathbf{u}) = D\nabla^2 \phi - \tau_D \nabla \cdot \left(\phi \frac{\partial \mathbf{u}}{\partial t} \right) + \mathcal{O}(Ma^3), \tag{29}$$

where the diffusion coefficient is given by $D = \tau_D/3$. The last term on the right hand side of equation (29) gives rise to a numerical (artificial) diffusion term which should ideally be eliminated or minimised. This will be addressed in Section 5.

3.1 The lattice Boltzmann equations

Content that the discrete velocity Boltzmann equations (11) and (12) furnish the governing equations in the macroscopic and incompressible limit, we proceed to discretise the model in space and time. To simplify the procedure we define new equilibria

$$f_i^{(0)} = f_i^{(eq)} + \tau_\nu R_i, \tag{30}$$

so that the discrete Boltzmann equation (11) can be written as

$$\frac{\partial f_i}{\partial t} + \mathbf{c}_i \cdot \nabla f_i = -\frac{1}{\tau_\nu} \left(f_i - f_i^{(0)} \right). \tag{31}$$

Integrating equation (31) along a characteristic for time yields

$$f_i(\mathbf{x} + \mathbf{c}_i \Delta t, t + \Delta t) - f_i(\mathbf{x}, t) = \int_0^{\Delta t} \Omega_i(x + c_i s, t + s) ds, \tag{32}$$

where Ω_i represents the collision term on the right hand side of equation (31). It should be noted that the left hand side of equation (32) is *exact*. The right hand side can be approximated using the Trapezium rule, which yields a second order accurate but implicit system of algebraic equations:

$$f_i(\mathbf{x}+\mathbf{c}_i\Delta t, t+\Delta t) - f_i(\mathbf{x}, t) = \frac{\Delta t}{2} \Big(\Omega_i(\mathbf{x}+\mathbf{c}_i\Delta t, t+\Delta t) \\ + \Omega_i(\mathbf{x}, t) \Big) + \mathcal{O}\left(\Delta t^3\right). \tag{33}$$

Following He *et al.* [23], we introduce the new variables

$$\bar{f}_i(\mathbf{x}, t) = f_i(\mathbf{x}, t) + \frac{\Delta t}{2\tau_\nu} \left(f_i(\mathbf{x}, t) - f_i^{(0)}(\mathbf{x}, t) \right). \tag{34}$$

The previous implicit scheme (33) can now be expressed as explicit formulae for the new variables, $\bar{f}_i$, at the new timestep:

$$\overline{f}_i(\mathbf{x} + \mathbf{c}_i\Delta t, t + \Delta t) - \overline{f}_i(\mathbf{x}, t) = -\frac{\Delta t}{\tau_\nu + \Delta t/2} \left(\overline{f}_i(\mathbf{x}, t) - f_i^{(0)}(\mathbf{x}, t) \right). \tag{35}$$

We thus discard the f_i and instead evolve the $\overline{f}_i$ using (35). The hydrodynamic moments must be obtained from moments of $\overline{f}_i$. The equilibrium function (13) depends on moments of f_i, not $\overline{f}_i$. Density is conserved and unaffected by the source term, R_i, and can thus be obtained just as easily from $\overline{f}_i$ as it can from f_i: $\rho = \sum_i f_i = \sum_i \overline{f}_i$. The velocity, $\mathbf{u}$, however, must be reconstructed from the first-order moment of $\overline{f}_i$:

$$\rho\bar{\mathbf{u}} = \sum_i \overline{f}_i \mathbf{c}_i = \rho\mathbf{u} - \frac{\Delta t}{2}\mathbf{F}. \tag{36}$$

The same method of discretisation applied to equation (12) yields the lattice Boltzmann equation for $\bar{g}_i$,

$$\bar{g}_i\left(\mathbf{x} + \mathbf{c}_i\Delta t, t + \Delta t\right) - \bar{g}_i(\mathbf{x}, t) = -\frac{\Delta t}{\tau_D + \Delta t/2}\left(\bar{g}_i(\mathbf{x}, t) - g_i^{(eq)}(\mathbf{x}, t)\right), \qquad (37)$$

where

$$\bar{g}_i\left(\mathbf{x}, t\right) = g_i\left(\mathbf{x}, t\right) + \frac{\Delta t}{2\tau_D}\left(g_i\left(\mathbf{x}, t\right) - g_i^{(eq)}\left(\mathbf{x}, t\right)\right), \qquad (38)$$

and $g_i^{(eq)}$ is given in equation (14).

4   Boundary conditions

We consider solid boundaries to be located precisely at grid points. Each boundary lattice node must supply incoming distribution functions to the flow domian. For example, a horizontal wall located along the bottom row of the computational domain has three incoming (unknown) fluid distribution functions, $\overline{f}_2$, $\overline{f}_5$ and $\overline{f}_6$, as shown in Figure 2. There is just one unknown temperature distribution function, $\bar{g}_2$, here. All other distribution functions at the boundary are known from the algorithms (35) and (37). To solve for the unknowns we need an equal number of linearly independent equations.

The moment-based method of Bennett [4] is an extension and generalisation of the method of Noble *et al.* [38] which formulates the boundary conditions in terms of the moments of the distribution functions, rather than on the distribution functions directly. Natural convection in a cavity (Figure 3) requires two types of boundary conditions: Dirichlet and Neumann. The solid boundaries are impermeable, rigid and stationary, and subjected to the no–slip condition. The combinations of the unknown $\overline{f}_i$ that appear in each of the moments at horizontal and vertical walls are shown in Table 1 and Table 2, respectively, where $\bar{S}_{xxyy} = \sum_i \overline{f}_i c_{ix}^2 c_{iy}^2$. Our three linearly independent equations are obtained by choosing three moments, one from each row of the appropriate table, and imposing boundary conditions upon these moments. The three equations can then be solved for the three unknowns in terms of the moment constraints and the known distributions. Since we are computing the Navier–Stokes equations, it is logical to choose the hydrodynamic moments: the two components of momentum and the remaining independent component of the momentum flux. The no–slip and no–flow boundary conditions state $u_x = u_y = 0$, and require the tangential derivative of the tangential component of velocity to vanish at a solid boundary, $\partial_T u_T = 0$, where T denotes the tangential component. By equations (23), (27), (28), and remembering that $u_T = 0$, this third condition can be expressed as $\Pi_{TT} = \Pi_{TT}^{(0)} = \rho/3$. It is now simple to solve the resulting equations for the three incoming distribution functions.

It is important to respect the variable transformation (34). That is, we place conditions on the flow variables, which must then be expressed in terms of 'barred' quantities. For a concrete example, let's consider a southern boundary. Using the above system of equations and constraints, we can compute the unknown $\overline{f}_i$ at a south wall by

$$\bar{f}_2 = \bar{f}_1 + \bar{f}_3 + \bar{f}_4 + 2(\bar{f}_7 + \bar{f}_8) - \frac{\rho}{3} - \frac{\Delta t}{2}F_y, \qquad (39)$$

$$\bar{f}_5 = -\bar{f}_1 - \bar{f}_8 + \frac{\rho}{6}, \tag{40}$$

$$\bar{f}_6 = -\bar{f}_3 - \bar{f}_7 + \frac{\rho}{6}. \tag{41}$$

The density, ρ, at the wall can be found in terms of the imposed velocity and the known distribution functions:

$$\rho = \rho \bar{u}_y + \overline{f}_0 + \overline{f}_1 + \overline{f}_3 + 2\left(\overline{f}_4 + \overline{f}_7 + \overline{f}_8\right). \tag{42}$$

Special attention must be paid to the corners, where there are five unknown $\overline{f}_i$. We simultaneously apply the conditions placed on the vertical and horizontal walls to give constraints on $\rho u_x, \rho u_y, \Pi_{xx}$ and Π_{yy}. The fifth constraint is $\Pi_{xy} = 0$, which eliminates the shear stress. An example of a southwest corner with its 5 unknown distributions is shown in Figure 2. Here the unknown $\overline{f}_i$ are found to be

$$\bar{f}_1 = \frac{2\rho}{3} - \bar{f}_0 - \bar{f}_3 - \frac{\Delta t}{2} F_y, \tag{43}$$

$$\bar{f}_2 = \frac{2\rho}{3} - \bar{f}_0 - \bar{f}_4, \tag{44}$$

$$\bar{f}_5 = -\frac{2\rho}{3} + \bar{f}_0 + \bar{f}_3 + \bar{f}_4 + \bar{f}_7 + \frac{\Delta t}{4} F_y, \tag{45}$$

$$\bar{f}_6 = \frac{\rho}{6} - \bar{f}_3 - \bar{f}_7, \tag{46}$$

$$\bar{f}_8 = \frac{\rho}{6} - \bar{f}_4 - \bar{f}_7 + \frac{\Delta t}{4} F_y, \tag{47}$$

where ρ is again found from known distribution functions at the wall.

The lattice Boltzmann equation for the thermal flow must supply one incoming $\bar{g}_i$ at the boundaries. For the heated walls the Dirichlet boundary condition can be realised by solving $\phi_{wall} = \sum_i g_i = \sum_i \bar{g}_i$ for the incoming $\bar{g}_i$. The Neumann boundary condition for the adiabatic walls require $\partial_N \phi = 0$, where ∂_N denotes the normal derivative. Since the temperature flux is found from the non–equilibrium part of g_i, and remembering that $\mathbf{u} = 0$, our one constraint is chosen to be $\Psi_N = \sum_i g_i c_{iN} = 0$, where c_{iN} is the normal component of the particle velocity. This reduces to simple 'bounce-back' for $\bar{g}_i$, and once we have found the incoming $\bar{g}_i$ we can compute the wall temperature needed for the force term in the boundary conditions for $\overline{f}_i$. We must supply two unknown $\bar{g}_i$ at the corners of the cavity, and these are found by applying the conditions on the vertical and horizontal walls simultaneously. We note again that this method does not require constraints to be placed on the collision operator in order to satisfy hydrodynamic boundary conditions.

5 Multiple relaxation times

To improve accuracy and numerical stability one should use a multiple relaxation time (MRT) collision operator [12, 29, 30, 13]. The construction of the MRT scheme for $\overline{f}_i$ presented here follows closely the model of Dellar [11], which forms an orthogonal basis in $\mathbb{R}^9$ by introducing the ghost moments

$$\bar{\mathcal{N}} = \sum_{i=0}^{8} H_i \overline{f}_i, \quad \bar{\mathcal{J}} = \sum_{i=0}^{8} H_i \overline{f}_i \mathbf{c}_i, \tag{48}$$

where $H_i = (1, -2, -2, -2, -2, 4, 4, 4, 4)^T$. The velocity distribution function $\overline{f}_i$ can now be expressed in terms of the nine independent moments

$$
\overline{f}_i = W_i \left(\rho + 3\rho \mathbf{u} \cdot \mathbf{c}_i + \frac{9}{2} \left(\overline{\overline{\Pi}} - \frac{\rho}{3} \mathbf{I} \right) : \left(\mathbf{c}_i \mathbf{c}_i - \frac{1}{3} \mathbf{I} \right) \right)
$$
$$
+ W_i H_i \left(\frac{1}{4} \bar{\mathcal{N}} + \frac{3}{8} \mathbf{c}_i \cdot \bar{\boldsymbol{\mathcal{J}}} \right). \tag{49}
$$

The equilibrium ghost moments are $\mathcal{N}^{(0)} = \mathcal{J}_\alpha^{(0)} = 0$, where α denotes the Cartesian components.

Each non–conserved moment is relaxed to equilibrium with its own collision time. In particular,

$$
\bar{\boldsymbol{\Pi}}' = \bar{\boldsymbol{\Pi}} - \frac{\Delta t}{\tau_\nu + \Delta t/2} \left(\bar{\boldsymbol{\Pi}} - \boldsymbol{\Pi}^{(0)} \right), \tag{50}
$$

$$
\bar{\mathcal{N}}' = \bar{\mathcal{N}} - \frac{\Delta t}{\tau_N + \Delta t/2} \left(\bar{\mathcal{N}} - \mathcal{N}^{(0)} \right), \tag{51}
$$

$$
\bar{\boldsymbol{\mathcal{J}}}' = \bar{\boldsymbol{\mathcal{J}}} - \frac{\Delta t}{\tau_J + \Delta t/2} \left(\bar{\boldsymbol{\mathcal{J}}} - \boldsymbol{\mathcal{J}}^{(0)} \right), \tag{52}
$$

where the primes denote post–collisional moments. The general MRT algorithm with moment–based boundary conditions is summarised as follows:

1. construct the moments of $\overline{f}_i$;

2. construct the equilibrium moments;

3. relax the non–conserved moments according to equations (50)–(51);

4. reconstruct the distribution function (49) using the post–collisional moments;

5. advect;

6. apply boundary conditions.

The moment–based boundary conditions discussed in Section 4 are free from numerical slip and allow us to choose the relaxation times for the ghost moments purely on the grounds of numerical stability. The numerical properties of the lattice Boltzmann algorithm are primarily controlled not by each individual relaxation time but by the product $\Lambda = \tau_\nu \tau_J$ [13]. One should determine τ_ν according to the non–dimensional numbers that characterise the flow (here the Rayleigh and Prandtl numbers) and fix τ_J according to Λ. The value $\Lambda = 1/4$ eliminates the recurrence of the non–equilibrium parts of the moments and gives the optimal stability [13]. Throughout this article we use $\Lambda = 1/4$ and $\tau_N = \tau_\nu$ (that is, a two–relaxation–time model).

The multiple relaxation time model for $\bar{g}_i$ is designed to minimise the numerical diffusion term in equation (29). We use the same model as Wang *et al.* [44] (but in terms of $\bar{g}_i$) which constructs the moments

$$
\begin{bmatrix} \phi \\ \bar{\phi u}_x \\ \bar{\phi u}_y \\ \bar{K}_{xx} \\ \bar{K}_{yy} \end{bmatrix} = \begin{bmatrix} 1 & 1 & 1 & 1 & 1 \\ 0 & 1 & 0 & 1 & 0 \\ 0 & 0 & 1 & 0 & 1 \\ -4 & 1 & 1 & 1 & 1 \\ 0 & 1 & -1 & 1 & -1 \end{bmatrix} \begin{bmatrix} \bar{g}_0 \\ \bar{g}_1 \\ \bar{g}_2 \\ \bar{g}_3 \\ \bar{g}_4 \end{bmatrix} \tag{53}
$$

with equilibria

$$\left[\phi, \phi u_x, \phi u_y, A\phi, 0\right].\tag{54}$$

A Chapman–Enskog analysis shows that the diffusion coefficient is now a function of the parameter A as well as the relaxation time for the temperature flux, $D = \tau_D(4 + A)/10$. Furthermore, to ensure that the numerical diffusion term is isotropic at fourth order, one should fix $\tau_D = \sqrt{3}/6$ and adjust A according to the Rayleigh and Prandtl numbers. The relaxation times for the ghost moments are $\tau_K = \sqrt{3}/3$ [44].

6   Natural convection in a square cavity

We study the benchmark problem of convection in a unit square cavity, as illustrated in Figure 3. The side walls have a fixed temperature and the top and bottom walls are insulated. All the walls are impermeable to fluid flow and are rigid, thus the no-slip boundary condition applies. To assess the accuracy of the proposed model we compute the volume averaged Nusselt number, the average Nusselt number along the hot wall, and the average Nusselt along the vertical centreline, which are defined to be

$$Nu = \int_x \int_y q_x \, dy \, dx, \quad Nu_0 = \int_y q_x \, dy|_{x=0}, \quad Nu_{1/2} = \int_y q_x \, dy|_{x=1/2}, \tag{55}$$

where q_x is the heat flux in the horizontal direction. We also compute the maximum and minimum Nusselt number along the hot wall.

Tables 3 and 4 show the data obtained on successive meshes with $Ma = 0.017$ and $Ma = 0.01$ (corresponding to $\Delta t/\Delta x = 0.01$ and 0.0058, respectively). In this section we study four different Rayleigh numbers, ranging from $Ra = 1000$ to $Ra = 1000000$. For a comparison with existing results in the literature we fixed the Prandtl number at $Pr = 0.71$. The entries "/" indicate that no data was able to be obtained. For the $Ra = 1000$ case in Table 3, the inability to obtain data is believed to be the due to compressibility effects in the moment–method, where we must calculate ρ at the wall. For these Ra numbers, the only other time we could not obtain data was when $Ra = 1000000$ on a very coarse 17×17 grid. The instability in this case is due to a negative value of the parameter A. Although some of the data obtained on the very coarse grids is clearly inaccurate, it is still interesting to note that the algorithm was stable and converged with such a large grid spacing, Δx. A comparison of Tables 3 and 4 show us that the Mach number Ma has little effect on the accuracy of the model at larger Ra (as also noted by Wang *et al.* [44]). The differences at smaller Ra are due to the residual compressibility (we note that the largest Ma number used here is larger than that in Wang *et al.* [44]). The magnitude of these differences rapidly decreases when we lower the Mach number further.

The data given in Tables 3 and 4 show the expected increase of the Nusselt numbers with Rayleigh number. A similar trend is observed in Table 5, which gives the value of the streamfunction at the cavity midpoint and the maximum value of the streamfunction for different Ra numbers. These are identical for $Ra = 1000$ and $Ra = 10000$ but differ at larger Rayleigh numbers, as is to be expected. The numerical predictions discussed above are seen to converge with second order accuracy. This observation is confirmed by Table 6, which shows the global L_2 error norm for the velocity, pressure, and temperature. The global L_2 error norm for velocity is defined to be

$$||\delta\mathbf{u}||_2 = \frac{\sum_{i,j} ||\mathbf{u}(\mathbf{x}) - \mathbf{u}^{REF}(\mathbf{x})||_2}{\sum_{i,j} ||\mathbf{u}^{REF}(\mathbf{x})||_2} \tag{56}$$

where $\mathbf{u}^{REF}$ is the reference data obtained on the finest grid. The L_2 error norms for pressure and temperature were computed in a similar way. The second order convergence rate shown in Table 6 for all flow fields confirms the consistency and robustness of our model.

Flow fields are plotted in Figure 4. The plots for the streamlines are coloured by the vertical component of velocity. Evidently, our lattice Boltzmann model is capturing the distinguishing flow patterns of natural convection in a cavity: at low Rayleigh numbers there is a dominant recirculating motion in the core region; and at higher Ra a prominent boundary layer develops along the wall. To assess the accuracy of the model we compare in Tables 7 and 8 our extrapolated results with benchmark data in the literature. An excellent agreement between the present and existing data sets is observed.

7 Higher Rayleigh numbers

We continue the verification of the lattice Boltzmann model with moment–based boundaries by considering flows with $Pr = 0.71$ at $Ra = 10^7$ and 10^8. Beyond this, the flow becomes unsteady in this configuration. Table 9 shows the Nusselt numbers at $Ra = 10^7$ and $Ra = 10^8$. We were unable to obtain data on very coarse meshes and the smallest grid used was 65×65 for $Ra = 10^7$ and 257×257 for $Ra = 10^8$. To enable us to conduct a mesh convergence study we simulated these flows in domains containing up to 1025^2 grid points. Our results are also compared with benchmark data. An excellent agreement is observed, especially with the highly accurate pseudo–spectral simulations of Le Quere [32]. We remind the reader that all data was obtained on uniform grids and no interpolation/extrapolation has been performed.

We present results for the streamfunction in Table 10 and plot the streamlines, isotherms, and pressure when $Ra = 10^8$ in Figure 5. Again, an excellent agreement with the pseudo–spectral data [32] is shown. The figures indicate a very thin boundary layer and little vertical motion far away from this in the bulk region. Convergence of the algorithm is observed in Table 11 to be second order, where the reference data is taken from a grid of size 1025^2 lattice points.

8 Convection in a partially heated cavity

For a final study we consider natural convection inside an air–filled square cavity, partially heated from below and cooled from the left. The geometry is as Figure 3 but the left wall is cold ($\theta(0, y) = 0$) and the right is perfectly insulated. The bottom wall is again adiabatic except in the region $1/2 - \epsilon/2 \leq x \leq 1/2 + \epsilon/2$, where $\theta(x, 0) = 1$ and $\epsilon = 0.2$. This flow is of relevance to the electronics industry and MEMS, where it is desirable to optimise the fluid circulation and cooling performance based on geometry in order the reduce the need for mechanical fans.

The flow fields are plotted in Figure 6. The background contours in the streamlines plot are coloured by the horizontal component of the velocity. The flow has a large roll-cell with a primary vortex region near the centre of the cavity and smaller internal vorticies

off-centre. Table 12 shows the computed Nusselt number $Nu_c = \int_0^1 \partial_x \phi|_{x=0} dy$ along the cold wall and the maximum value of both components of velocity for different mesh sizes. For comparison we also show the results obtained by Cianfrini *et al.* [8] on their finest mesh using a finite difference method. Once again, the lattice Boltzmann predictions are in good agreement with existing results. However, the difference between the two data sets is larger than in Section 6 and a few comments are in order. Firstly we should note that the percentage difference between our predictions on successive meshes is monotonically decreasing, whereas the grid sensitivity analysis in Cianfrini *et al.* [8] shows some non–monotonic behaviour. We would thus argue that our model is numerically robust to mesh refinements. Table 12 also shows that the maximum values of velocity converge with second order accuracy in space but the Nusselt number is converging with only first order. This is confirmed in Table 13 which gives the relative L_2 error for the velocity, pressure, and temperature. One can see that the global velocity error is decreasing like $\mathcal{O}(\Delta x^2)$, but the temperature like $\mathcal{O}(\Delta x)$. We are of the opinion that this decrease in accuracy of the ϕ is due to a lower order approximation of the temperature flux along the bottom wall, which is possibly enhanced by an insufficient initialisation procedure. This small but interesting anomaly is a topic for future research.

9 Conclusion

Boundary conditions for the lattice Boltzmann equation are most commonly applied using the bounce–back method. Despite its simplicity, bounce–back introduces a spurious slip velocity of order $\mathcal{O}(\Delta x^2)$ [16, 24]. To minimise this error without excessive mesh resolution, one must adjust the relaxation time of the third order moment according to the 'magic parameter' [16]. If this relationship between the relaxation times for the second and third order moments is satisfied, the lattice Boltzmann method can accurately simulate flow phenomena, including natural convection [44]. However, the need to eliminate the numerical slip associated with bounce–back places a restriction on the collision operator. In particular, the value of the magic parameter $\Lambda = 3/16$ is not necessarily optimal in terms of numerical stability [13]. Furthermore, hydrodynamic boundary conditions more complicated than no–slip are not easily satisfied by bounce–back and its variants.

We have presented an application of moment–based boundary conditions for the lattice Boltzmann equation for natural convection up to a Rayleigh number of $Ra = 10^8$. The moment–method was originally proposed by Bennett [4] and may be viewed as an extension and generalisation of Noble's method for hexagonal lattices [38]. Unlike all existing lattice Boltzmann boundary conditions, the moment–method is formulated purely in terms of hydrodynamic variables at grid points. The constrained moments at the wall are solved in terms of the unknown (incoming) discrete velocity distribution functions. The moment–method does not compromise the locality nor the order of accuracy of the lattice Boltzmann equation and allows us to evaluate flow variables precisely at grid points. There is no numerical slip error in the moment–method.

The method has been applied to the two distribution functions for a thermal MRT lattice Boltzmann model. The ghost relaxation times have been chosen in accordance with numerical stability analysis [13] and not to satisfy the no–slip condition. We have evaluated the model for natural convection in square cavities and assessed its accuracy. Our results for the Nusselt numbers and the streamfunction are in excellent agreement with benchmark data for all tested Rayleigh numbers. The algorithm is numerically stable on

coarse meshes and has been shown to converge with second order accuracy. As a first step towards solving industrially–relevant convection problems, we have also shown how easily the moment–method can be applied to partially heated convection problems. Our numerical investigation has shown that the moment–method can be a viable alternative to bounce–back for thermal flows in planar geometries, offering the possibility to incorporate more complicated boundary conditions into the lattice Boltzmann framework.

Acknowledgments

References

[1] C K. Aidun and J. R. Clausen. Lattice-Boltzmann Method for Complex Flows. *Annual Review of Fluid Mechanics*, 42(1):439–472, 2010.

[2] F. J. Alexander, S. Chen, and J. D. Sterling. Lattice Boltzmann Thermohydrodynamics. *Physical Review E*, 47(4):2249–2252, 1993.

[3] A. Bartoloni, C. Battista, S. Cabasino, P.S. Paolucci, J. Pech, R. Sarno, G.M. Todesco, M. Torelli, W. Tross, and P. Vicini. LBE simulations of Rayleigh-Benard convection on the APE100 parallel processor. *International Journal of Modern Physics C*, 4(5):993–1006, 1993.

[4] S. Bennett. *A Lattice Boltzmann Model for Diffusion of Binary Gas Mixtures*. PhD thesis, University of Cambridge, 2010.

[5] S. Chapman and T.G. Cowling. *The mathematical theory of non-uniform gases*. Cambridge University Press, 1939.

[6] S. Chen and G. D. Doolen. Lattice Boltzmann Method for fluid flows. *Annual review of fluid mechanics*, 30(1):329–364, 1998.

[7] S-K Choi and S-O Kim. Comparative Analysis of Thermal Models in the Lattice Boltzmann Method for the Simulation of Natural Convection in a Square Cavity. *Numerical Heat Transfer, Part B: Fundamentals*, 60(2):135–145, 2011.

[8] C. Cianfrini, M. Corcione, E. Habib, and A. Quintino. Convective Transport in Rectangular Cavities Partially Heated at the Bottom and Cooled at One Side. *Journal of Thermal Science*, 22(01):55–63, 2013.

[9] R. M. Clever and F. H. Busse. Transition to time-dependent convection. *Journal of Fluid Mechanics*, 65(04):625–645, 1974.

[10] G. de Vahl Davis. Natural convection of air in a square cavity: a benchmark numerical solution. *International Journal for Numerical Methods in Fluids*, 3:249–264, 1983.

[11] P. J. Dellar. Incompressible limits of lattice Boltzmann equations using multiple relaxation times. *Journal of Computational Physics*, 190(2):351–370, 2003.

[12] D. d'Humières. Generalized lattice Boltzmann equations. *Progress in Aeronautics and Astronautics*, 159:450–458, 1992.

[13] D. d'Humières and I. Ginzburg. Viscosity independent numerical errors for Lattice Boltzmann models: From recurrence equations to "magic" collision numbers. *Computers and Mathematics with Applications*, 58:823–840, 2009.

[14] H.N. Dixit and V. Babu. Simulation of high Rayleigh number natural convection in a square cavity using the lattice Boltzmann method. *International Journal of Heat and Mass Transfer*, 49(3):727–739, 2006.

[15] J. G. M. Eggels and J. A. Somers. Numerical simulation of free convective flow using the lattice-Boltzmann scheme. *International Journal of Heat and Fluid Flow*, 16(5):357–364, 1995.

[16] I. Ginzbourg and M. P. Adler. Boundary flow condition analysis for the three-dimensional lattice Boltzmann model. *Journal de Physique II*, 4:191–214, 1994.

[17] Z. Guo, B. Shi, and C. Zheng. A coupled lattice BGK model for the Boussinesq equations. *International Journal for Numerical Methods in Fluids*, 39(4):325–342, 2002.

[18] Z. Guo, C. Zheng, B. Shi, and T. Zhao. Thermal lattice Boltzmann equation for low Mach number flows: Decoupling model. *Physical Review E*, 75(3):036704–1–036704–15, 2007.

[19] X. He, S. Chen, and G. D. Doolen. A Novel Thermal Model for the Lattice Boltzmann Method in Incompressible Limit. *Journal of Computational Physics*, 146(1):282–300, 1998.

[20] X. He and L-S. Luo. Lattice Boltzmann Model for the Incompressible NavierâŁ"Stokes Equation. *Journal of Statistical Physics*, 88(3/4):927–944, 1997.

[21] X. He and L-S. Luo. Theory of the lattice Boltzmann method: From the Boltzmann equation to the lattice Boltzmann equation. *Physical Review E*, 56:6811–6817, 1997.

[22] X. He, L-S. Luo, and M. Dembo. Some Progress in Lattice Boltzmann Method. Part I. Nonuniform Mesh Grids. *Journal of Computational Physics*, 129(2):357–363, 1996.

[23] X. He, X. Shan, and G. Doolen. Discrete Boltzmann equation model for nonideal gases. *Physical Review E*, 57(1):13–16, 1998.

[24] X. He, Q. Zou, L-S. Luo, and M. Dembo. Analytic Solutions of Simple Flows and Analysis of Nonslip Boundary Conditions for the Lattice Boltzmann BGK Model. *Journal of Statistical Physics*, 87:115–136, 1997.

[25] R. A. W. M. Henkes and C. J. Hoogendoorn. Scaling of the laminar natural-convection flow in a heated square cavity. *International Journal of Heat and Mass Transfer*, 36(11):2913–2925, 1993.

[26] M. Hortmann, M. Peric, and G. Scheuerer. Finite volume multigrid prediction of laminar natural convection: benchmark solutions. *International Journal for Numerical Methods in Fluids*, 11:189–207, 1990.

[27] T. Inamuro, M. Yoshino, and F. Ogino. A non-slip boundary condition for lattice Boltzmann simulations. *Physics of Fluids*, 7(12):2928–2930, 1995.

[28] S-J. Kim, F. Wang, M. Burns, and K. Kurabayashi. Temperature–Programmed Natural Convection for Micromixing and Biochemical Reaction in a Single Microfluidic Chamber. *Analytical Chemistry*, 11(81):4510–4516, 2009.

[29] A.J.C. Ladd. Numerical simulations of particulate suspensions via a discretized Boltzmann equation. Part 1. Theoretical foundation. *Journal of Fluid Mechanics*, 271:258–309, 1994.

[30] P. Lallemand and L-S. Luo. Theory of the lattice Boltzmann method: Dispersion, dissipation, isotropy, Galilean invariance, and stability. *Physical Review E*, 61:6546–6562, 2000.

[31] P. Lallemand and L-S. Luo. Hybrid Finite-Difference Thermal Lattice Boltzmann Equation. *International Journal of Modern Physics B*, 17(1-2):41–47, 2003.

[32] P. Le Quere. Accurate solutions to the square thermally driven cavity at high Rayleigh number. *Computers & Fluids*, 20(1):29–41, 1991.

[33] Q. Li, K. H. Luo, Y. L. He, Y. J. Gao, and W. Q. Tao. Coupling lattice Boltzmann model for simulation of thermal flows on standard lattices. *Physical Review E*, 85(1):016710, 2012.

[34] L-S. Luo. Unified Theory of Lattice Boltzmann Models for Nonideal Gases. *Physical Review Letters*, 81:1618–1621, 1998.

[35] N.C. Markatos and K.A. Pericleous. Laminar and turbulent natural convection in an enclosed cavity. *International Journal of Heat and Mass Transfer*, 27(5):755–772, 1984.

[36] G. R. McNamara, A. L. Garcia, and B. J. Alder. Stabilization of thermal lattice Boltzmann models. *Journal of Statistical Physics*, 81(1-2):395–408, 1995.

[37] A. Mezrhab, M. Bouzidi, and P. Lallemand. Hybrid lattice-Boltzmann finite-difference simulation of convective flows. *Computers & Fluids*, 33(4):623–641, 2004.

[38] D. R. Noble, S. Chen, J. N. Chen, J. H. Georgiadis, and R. O Buckius. A consistent hydrodynamic boundary condition for the lattice Boltzmann method. *Physics of Fluids*, 7:203–209, 1995.

[39] Y.H. Qian, D. d'Humières, and P. Lallemand. Lattice BGK Models for Navier-Stokes Equation. *Europhysics Letters*, 17:479–484, 1992.

[40] T Reis and P.J. Dellar. Lattice Boltzmann simulations of pressure-driven flows in microchannels using Navier–Maxwell slip boundary conditions. *Physics of Fluids*, 24(11):112001, 2012.

[41] X. Shan. Simulation of Rayleigh-Benard convection using a lattice Boltzmann method. *Physical Review E*, 55(3):2780–2788, 1997.

[42] J. M. Wallace and P. V. Hobbs. *Atmospheric science: an introductory survey*. Academic press, second edition, 2006.

[43] D.C. Wan, B.S.V. Patnaik, and G.W. Wei. A new benchmark quality solution for the buoyancy–driven cavity by discrete singular convection. *Numerical Heat Transfer Part B*, 40:199–228, 2001.

[44] J Wang, D Wang, P Lallemand, and L-S Luo. Lattice Boltzmann simulations of thermal convective flows in two dimensions. *Computers & Mathematics with Applications*, 65(2):262–286, 2013.

[45] D. Yu, R. Mei, L-S. Luo, and W. Shyy. Viscous flow computations with the method of lattice Boltzmann equation. *Progress in Aerospace Sciences*, 39(5):329–367, 2003.
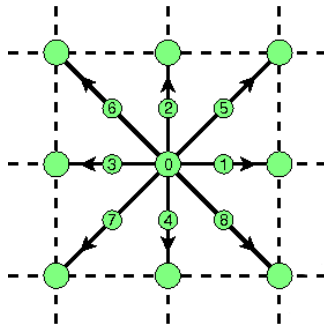
Figure 1 The D2Q9 lattice. The D2Q5 lattice does not have the diagonal links. Figure adapted from [40].
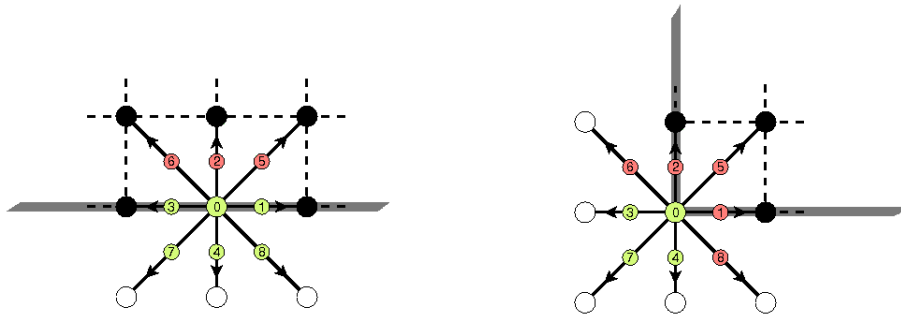

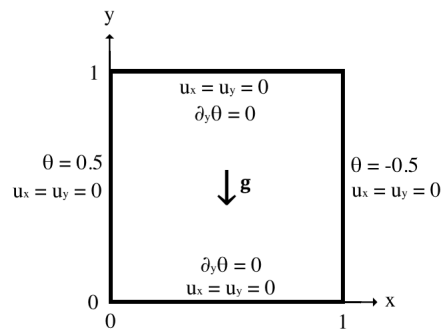**Figure 2** Unknown (incoming) distributions at a south wall (left) and a southwest corner (right).

Figure 3 Geometry and boundary conditions for square cavity problem.
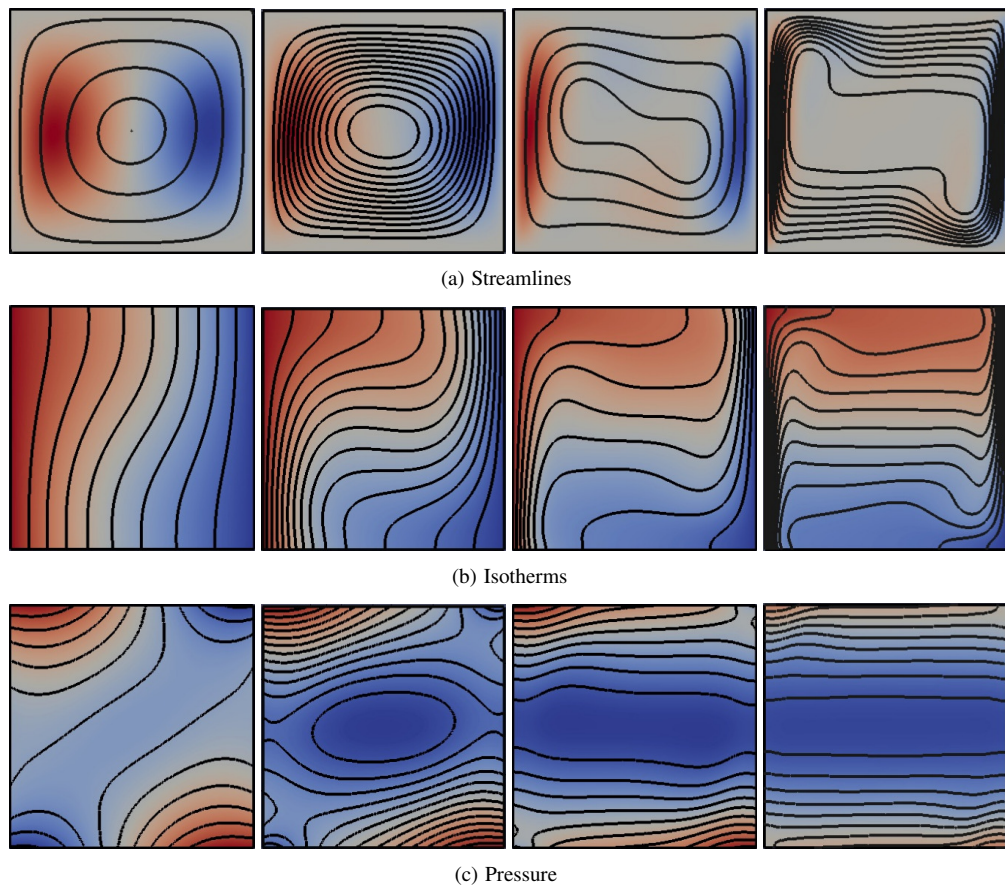
(a) Streamlines

(b) Isotherms

(c) Pressure

Figure 4   Contours of flow fields for convection in a square cavity. From left to right, $Ra = 1000$, $Ra = 10000$, $Ra = 100000$, $Ra = 1000000$.
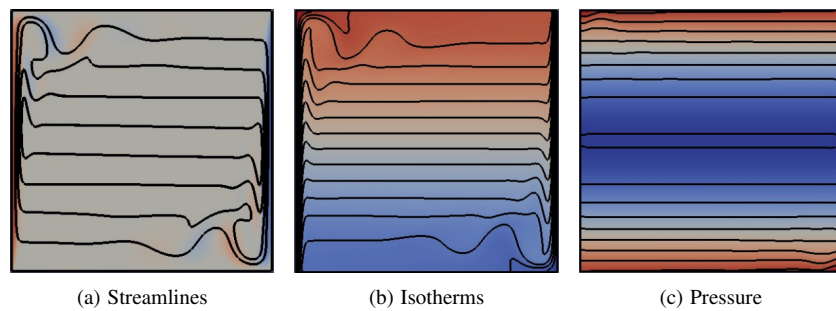

(a) Streamlines   (b) Isotherms   (c) Pressure

Figure 5   Contours of flow fields for convection in a square cavity at $Ra = 10^8$.

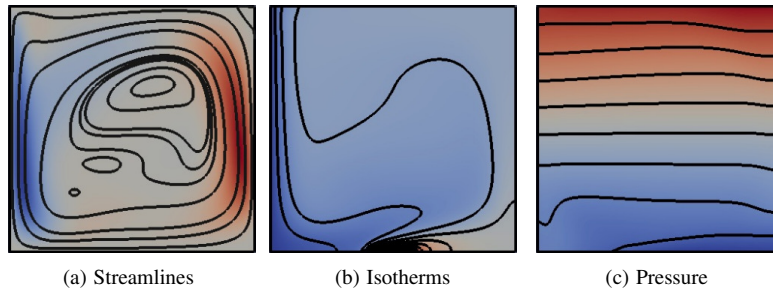(a) Streamlines   (b) Isotherms   (c) Pressure

Figure 6 Contours of flow fields for convection in a partially heated cavity.

Moments	Combination of unknowns at South boundary	Combination of unknowns at North boundary
$\rho,\quad \rho\bar{u}_y,\quad \bar{\Pi}_{yy}$	$\overline{f}_2 + \overline{f}_5 + \overline{f}_6$	$\overline{f}_4 + \overline{f}_7 + \overline{f}_8$
$\rho\bar{u}_x,\quad \bar{\Pi}_{xy},\quad \bar{Q}_{xyy}$	$\overline{f}_5 - \overline{f}_6$	$\overline{f}_7 - \overline{f}_8$
$\bar{\Pi}_{xx},\quad \bar{Q}_{xxy},\quad \bar{S}_{xxyy}$	$\overline{f}_5 + \overline{f}_6$	$\overline{f}_7 + \overline{f}_8$

Table 1 Moment groups for a south and north boundary

Moments	Combination of unknowns at East boundary	Combination of unknowns at West boundary
$\rho,\quad \rho\bar{u}_x,\quad \bar{\Pi}_{xx}$	$\overline{f}_3 + \overline{f}_6 + \overline{f}_7$	$\overline{f}_1 + \overline{f}_5 + \overline{f}_8$
$\rho\bar{u}_y,\quad \bar{\Pi}_{xy},\quad \bar{Q}_{xxy}$	$\overline{f}_6 - \overline{f}_7$	$\overline{f}_5 - \overline{f}_8$
$\bar{\Pi}_{yy},\quad \bar{Q}_{xyy},\quad \bar{S}_{xxyy}$	$\overline{f}_6 + \overline{f}_7$	$\overline{f}_5 + \overline{f}_8$

Table 2 Moment groups for an east and west boundary

Ra	$N_x \times N_y$	Nu	Nu_0	$Nu_{1/2}$	Nu_{max}	Nu_{min}
	17×17	1.11472	1.11814	1.20071	1.61093	0.59740
	33×33	1.11696	1.11754	1.11837	1.53025	0.66910
10^3	65×65	1.11757	1.11766	1.11793	1.60973	0.68610
	129×129	1.11773	1.11774	1.11783	1.50716	0.68991
	257×257	1.11777	1.11778	1.11780	1.50650	0.69089
	513×513	/	/	/	/	/
	17×17	2.24086	2.29969	2.24927	4.11321	-0.02887
	33×33	2.24303	2.25693	2.24603	3.65732	0.44114
10^4	65×65	2.24426	2.24641	2.24512	3.56119	0.55175
	129×129	2.24466	2.24495	2.24488	3.53808	0.57697
	257×257	2.24476	2.24481	2.24480	3.53276	0.58286
	513×513	2.24479	2.24481	2.24479	3.53148	0.58435
	17×17	4.51430	4.66560	4.46220	8.71591	4.72630
	33×33	4.52752	4.65051	4.51964	8.96233	0.27732
10^5	65×65	4.52250	4.54914	4.52166	8.01192	0.49053
	129×129	4.52178	4.52575	4.52168	7.79032	0.67206
	257×257	4.52165	4.52216	4.52163	7.73639	0.71423
	513×513	4.52163	4.52172	4.52163	7.72402	0.72429
	17×17	/	/	/	/	/
	33×33	8.90696	9.30568	8.86264	18.98663	-9.05280
10^6	65×65	8.85030	9.07902	8.84397	20.33165	-0.65955
	129×129	8.83097	8.87856	8.83037	18.28118	0.58184
	257×257	8.82651	8.83367	8.82641	17.71768	0.88363
	513×513	8.82539	8.82646	8.825289	17.57820	0.95559

Table 3 Nusselt numbers for convection in a cavity with $Pr = 0.71$ and $Ma = 0.017$. '/' denotes no data could be obtained.

Ra	$N_x \times N_y$	Nu	Nu_0	$Nu_{1/2}$	Nu_{max}	Nu_{min}
10^3	17×17	1.11475	1.11817	1.12009	1.61096	0.68996
	33×33	1.11695	1.11755	1.11830	1.53030	0.66940
	65×65	1.11758	1.11766	1.11793	1.50971	0.68633
	129×129	1.11774	1.11775	1.11782	1.50717	0.69004
	257×257	1.11778	1.11778	1.11778	1.50652	0.69091
	513×513	1.11779	1.11779	1.11779	1.50636	0.69116
10^4	17×17	2.24098	2.29983	2.24937	4.11339	-0.02687
	33×33	2.24307	2.25699	2.24607	3.65742	0.44218
	65×65	2.24427	2.24642	2.24513	3.56119	0.55228
	129×129	2.24466	2.244967	2.24487	3.53808	0.57725
	257×257	2.24477	2.24482	2.24481	3.53276	0.58301
	513×513	2.24480	2.24482	2.24480	3.53148	0.58443
10^5	17×17	4.51470	4.6661	4.46250	8.71631	-4.4723
	33×33	4.52764	4.65068	4.51976	8.96268	0.28395
	65×65	4.52226	4.54914	4.52173	8.01197	0.4549
	129×129	4.52179	4.52578	4.52168	7.79034	0.67295
	257×257	4.52166	4.52220	4.52165	7.73640	0.71469
	513×513	4.52164	4.52171	4.52164	7.72402	0.72451
10^6	17x17	/	/	/	/	/
	33×33	8.90735	9.30616	8.86301	18.9873	-9.03869
	65×65	8.85041	9.07916	8.84407	20.33220	-0.65411
	129×129	8.83108	8.87860	8.83049	18.28123	0.58460
	257×257	8.82667	8.83368	8.82668	17.71770	0.88506
	513×513	8.82570	8.82646	8.82583	17.57820	0.95634

Table 4 Nusselt numbers for convection in a cavity with $Pr = 0.71$ and $Ma = 0.01$. '/' denotes no data could be obtained. '/' denotes no data was obtained.

Ra	$N_x \times N_y$	$|\Psi_{mid}|$	$|\Psi_{max}|$
10^3	17×17	1.1530	1.1530
	33×33	1.1692	1.1692
	65×65	1.1733	1.1733
	129×129	1.1743	1.1743
	257×257	1.1746	1.1746
	513×513	1.1746	1.1746
10^4	17×17	5.0093	5.0093
	33×33	5.0569	5.0569
	65×65	5.0694	5.0694
	129×129	5.0726	5.0726
	257×257	5.0734	5.0734
	513×513	5.0736	5.0736
10^5	17×17	8.9901	9.5510
	33×33	9.0504	9.5770
	65×65	9.0983	9.6044
	129×129	9.1113	9.6139
	257×257	9.1145	9.6162
	513×513	9.1153	9.6167
10^6	17×17	/	/
	33×33	16.2595	16.6078
	65×65	16.3197	16.7071
	129×129	16.3692	16.7839
	257×257	16.3824	16.8038
	513×513	16.3860	16.8098

Table 5 The value of the streamfunction at the cavity midpoint and the maximum value of the streamfunction for convection in a cavity. $Pr = 0.71$, $Ma = 0.01$. '/' denotes no data was obtained.

Ra	10^3	10^4	10^5	10^6
$N_x \times N_y$		$\|\|\partial\mathbf{u}\|\|_2$		
17×17	3.8378×10^{-3}	9.1547×10^{-3}	5.0138×10^{-2}	/
33×33	9.9338×10^{-4}	2.2051×10^{-3}	1.0162×10^{-2}	6.9697×10^{-2}
65×65	2.4786×10^{-4}	5.4122×10^{-4}	2.4145×10^{-3}	1.5226×10^{-2}
129×129	5.9270×10^{-5}	1.2735×10^{-4}	5.7055×10^{-4}	3.5222×10^{-3}
257×257	1.0565×10^{-5}	2.4951×10^{-5}	1.1394×10^{-4}	6.9953×10^{-4}
		$\|\|\partial p\|\|_2$		
17×17	1.9747×10^{-4}	2.8808×10^{-4}	5.6873×10^{-4}	/
33×33	2.3928×10^{-5}	5.4801×10^{-5}	1.2527×10^{-4}	2.3457×10^{-4}
65×65	4.5027×10^{-6}	1.0606×10^{-5}	2.4002×10^{-5}	5.4268×10^{-5}
129×129	1.5225×10^{-6}	2.2072×10^{-6}	6.6312×10^{-6}	1.2545×10^{-5}
257×257	1.3833×10^{-7}	4.1803×10^{-7}	1.3608×10^{-6}	2.3763×10^{-6}
		$\|\|\partial\phi\|\|_2$		
17×17	5.7971×10^{-3}	1.9711×10^{-2}	5.5311×10^{-2}	/
33×33	1.4877×10^{-3}	5.1686×10^{-3}	1.3157×10^{-2}	4.1906×10^{-2}
65×65	3.7060×10^{-4}	1.2948×10^{-3}	3.3174×10^{-3}	9.9381×10^{-3}
129×129	8.8551×10^{-5}	3.0982×10^{-4}	7.9399×10^{-4}	2.3559×10^{-3}
257×257	1.7869×10^{-5}	6.2417×10^{-5}	1.5892×10^{-4}	4.7023×10^{-4}

Table 6 L_2 error norms for velocity, pressure, and temperature for convection in a cavity. $Pr = 0.71$ and $Ma = 0.01$. '/' denotes no data was obtained.

Ra	Study	Nu	Nu_0	$Nu_{1/2}$	Nu_{max}	Nu_{min}
10^3	Present	1.1178	1.1178	1.1178	1.5063	0.6914
	Wang *et al.* [44]	1.1178	1.1178	1.1178	1.5063	0.6912
	de Vahl Davis [10]	1.118	1.117	1.118	1.505	0.692
	Guo *et al.* [17]	-	1.1168	-	1.5004	-
	Dixit and Babu [14]	1.121	1.1272	1.118	-	-
10^4	Present	2.2448	2.2448	2.2448	3.5302	0.5856
	Wang *et al.* [44]	2.2448	2.2448	2.2448	3.5310	0.5849
	de Vahl Davis [10]	2.243	2.238	2.243	3.528	0.586
	Hortmann *et al.* [26]	2.24475	-	-	3.53087	-
	Guo *et al.* [17]	-	2.2477	-	3.5715	-
	Dixit and Babu [14]	2.286	2.247	2.256	-	-
10^5	Present	4.5216	4.5212	4.5216	7.7116	0.7343
	Wang *et al.* [44]	4.5216	4.5214	4.5216	7.7161	0.7279
	Mezrab *et al.* [37]	4.521	-	-	-	-
	de Vahl Davis [10]	4.519	4.509	4.519	7.717	0.729
	Hortmann *et al.* [26]	4.52164	-	-	7.72013	-
	Guo *et al.* [17]	-	4.5345	-	7.7951	-
	Dixit and Babu [14]	4.5463	4.5226	4.519	-	-
10^6	Present	8.8249	8.8192	8.8250	17.4387	0.9895
	Wang *et al.* [44]	8.8253	8.8192	8.8254	17.5274	0.9769
	Le Quere [32]	8.8252	-	8.8252	17.5360	0.97946
	Mezrab *et al.* [37]	8.824	-	-	-	-
	de Vahl Davis [10]	8.800	8.817	8.799	17.925	0.989
	Hortmann *et al.* [26]	8.82513	-	-	17.536	-
	Guo *et al.* [17]	-	8.7775	-	17.4836	-
	Dixit and Babu [14]	8.652	8.805	8.5074	-	-

Table 7 Comparison of Nusselt number results from different studies on square cavity convection.

Ra	Method	$|\Psi_{mid}|$	$|\Psi_{max}|$
	Present	1.1746	1.1746
10^3	Wang *et al.* [44]	1.1746	1.1746
	de Vahl Davis [10]	1.174	1.174
	Present	5.0738	5.0738
10^4	Wang *et al.* [44]	5.0737	5.0737
	de Vahl Davis [10]	5.0737	5.0737
	Present	9.1161	9.6721
10^5	Wang *et al.* [44]	9.1157	9.6179
	de Vahl Davis [10]	9.111	9.612
	Present	16.3890	16.8158
10^6	Wang *et al.* [44]	16.3868	16.8149
	Le Quere [32]	16.3864	16.8111
	de Vahl Davis [10]	16.32	16.750

Table 8 Comparison of streamfunction results from different studies on square cavity convection.

Ra	$N_x \times N_y$	Nu	Nu_0	$Nu_{1/2}$	Nu_{max}	Nu_{min}
	65×65	16.88755	17.57645	16.87737	43.79111	-2.32421
	129×129	16.60153	16.98110	16.59980	49.16712	-1.77141
	257×257	16.54184	16.62034	16.54164	43.33952	0.48276
10^7	513×513	16.52771	16.53985	16.52770	40.34342	1.41714
	1025×1025	16.52496	16.52570	16.52546	39.62226	1.31032
	Le Quere [32]	16.523	-	16.523	39.3947	1.36635
	Dixit and Babu [14]	16.79	-	-	-	-
	257×257	30.37062	30.96480	30.36674	108.6155	-0.34501
	513×513	30.25930	30.37972	30.25897	97.25299	0.77426
10^8	1025×1025	30.23339	30.25111	30.23347	89.68699	1.59352
	Le Quere [32]	30.225	-	30.225	87.2355	1.91907
	Dixit and Babu [14]	30.506	-	-	-	-

Table 9 Nusselt numbers for convection in a cavity with $Pr = 0.71$ and $Ma = 0.01$.

Ra	$N_x \times N_y$	$|\Psi_{mid}|$	$|\Psi_{max}|$
	65×65	29.5343	30.1304
	129×129	29.3386	30.0820
	257×257	29.3541	30.1409
10^7	513×513	29.3597	30.1583
	1025×1025	29.3639	30.1631
	Le Quere [32]	29.36	30.16
	Wang *et.al.* [43]	28.23	-
	257×257	52.2887	53.6390
	513×513	52.3133	53.7997
10^8	1025×1025	52.3208	53.8352
	Le Quere [32]	52.2322	53.8475
	Wang *et.al.* [43]	50.81	-

Table 10 The value of the streamfunction at the cavity midpoint and the maximum value of the streamfunction for convection in a cavity. $Pr = 0.71$, $Ma = 0.01$.

Ra	10^7	10^8
$N_x \times N_y$		$||\partial\mathbf{u}||_2$
65×65	1.4522×10^{-1}	/
129×129	4.0732×10^{-2}	/
257×257	9.9766×10^{-3}	8.6717×10^{-2}
513×513	2.0087×10^{-3}	2.1006×10^{-2}
		$||\partial p||_2$
65×65	1.1701×10^{-4}	/
129×129	2.5446×10^{-5}	/
257×257	5.7786×10^{-6}	9.5022×10^{-6}
513×513	1.1096×10^{-6}	1.8056×10^{-6}
		$||\partial\phi||_2$
65×65	7.6525×10^{-2}	/
129×129	1.7937×10^{-2}	/
257×257	4.2262×10^{-3}	1.5639×10^{-2}
513×513	8.4280×10^{-4}	3.1467×10^{-3}

Table 11 L_2 error norms for velocity, pressure, and temperature for convection in a cavity at high Rayleigh numbers. The reference solution is the results obtained on a 1025^2 mesh. '/' denotes no data was obtained.

$N_x \times N_y$	Nu_c	U_{max}	V_{max}
21×21	4.0676	268.32	307.67
41×41	3.9527	216.97	294.42
81×81	3.8656	201.57	287.11
161×161	3.8219	197.14	284.74
321×321	3.8041	195.81	284.13
641×641	3.7958	195.48	283.981
Cianfrini *et al.* [8]	3.726	194.40	281.27

Table 12 Average Nusselt number along the cold wall and maximum values for the velocity in a partially heated cavity. The table also shows the dependency of the results on the mesh, and a comparison with the finite difference results of Cianfrini *et al.* on their finest grid. $Pr = 0.71$, $Ra = 1000000$ and $Ma = 0.017$.

$N_x \times N_y$	$||\partial\mathbf{u}||_2$	$||\partial p||_2$	$||\partial\phi||_2$
21×21	3.538×10^{-1}	2.008×10^{-2}	8.974×10^{-2}
41×41	8.177×10^{-2}	3.037×10^{-3}	3.510×10^{-2}
81×81	2.192×10^{-2}	3.728×10^{-4}	1.687×10^{-2}
161×161	6.451×10^{-3}	7.144×10^{-5}	7.645×10^{-3}
321×321	1.720×10^{-3}	2.676×10^{-5}	2.606×10^{-3}

Table 13 L_2 error norms of velocity, pressure, and temperature in a partially heated cavity.